Bifurcations to transient and oscillatory excitations in inhomogeneous excitable media: Insights into arrhythmogenesis in long QT syndrome

Jianying Lin,[1] Zhilin Qu,[2] and Xiaodong Huang[1,*]
[1]*Department of Physics, South China University of Technology, Guangzhou 510641, China*
[2]*Department of Medicine, University of California, Los Angeles, Los Angeles, California 90095, USA*

(Received 1 September 2022; revised 26 December 2022; accepted 21 February 2023; published 10 March 2023)

Ventricular arrhythmias are the leading cause of sudden cardiac death. Understanding the mechanisms of arrhythmia initiation is important for developing effective therapeutics for prevention. Arrhythmias can be induced via premature external stimuli or occur spontaneously via dynamical instabilities. Computer simulations have shown that a large repolarization gradient due to regional prolongation of the action potential duration can result in instabilities leading to premature excitations and arrhythmias, but the bifurcation remains to be elucidated. In this study we carry out numerical simulations and linear stability analyses using a one-dimensional heterogeneous cable consisting of the FitzHugh-Nagumo model. We show that a Hopf bifurcation leads to local oscillations, which, once their amplitudes are large enough, lead to spontaneous propagating excitations. Depending on the degree of heterogeneities, these excitations can range from one to many and to be sustained oscillations, manifesting as premature ventricular contractions (PVCs) and sustained arrhythmias. The dynamics depends on the repolarization gradient and the length of the cable. Complex dynamics is also induced by the repolarization gradient. The mechanistic insights from the simple model may help in the understanding of the genesis of PVCs and arrhythmias in long QT syndrome.

DOI: 10.1103/PhysRevE.107.034402

I. INTRODUCTION

The heart is an excitable media in which regular conducting electrical excitations in the ventricles result in contractions to pump oxygenated blood to the whole body. When the electrical excitations become irregular and localized, such as focal excitations and spiral waves, ventricular arrhythmias occur, which is the major cause of sudden cardiac death [1,2]. While the mechanisms of arrhythmias, in particular the dynamics of abnormal electrical conduction and spiral waves, have been widely investigated [3–5], how the arrhythmia events are initiated in the heart remains incompletely understood.

A well-known phenomenon linking to arrhythmia initiation is called *R*-on-*T* on the electrocardiogram (ECG) [6–9]. As shown in Fig. 1(a), an early *R* wave is superimposed on the *T* wave of the previous beat, leading to ventricular arrhythmias. Two initiation mechanisms of ventricular arrhythmias linked to the *R*-on-*T* phenomenon are known [10,11]. One is reentry initiation via trigger and substrate interactions. In this mechanism, a trigger is an *R* wave that originates locally in the ventricles before the sinus beat, called premature ventricular contraction (PVC). A substrate is a tissue condition in which heterogeneities in repolarization are large. When a PVC occurs early enough, its conduction may be locally blocked in the heterogeneous region, leading to reentry or spiral waves. The other one is a spontaneous behavior in which a tissue-scale instability results in the formation of PVCs and reentry. In this mechanism, the PVC is caused by an enhanced repolarization gradient due to regional prolongation of the action potential duration [Fig. 1(b)], which can manifest as focal excitations or degenerate into reentry.

The *R*-on-*T* phenomenon is common in arrhythmogenesis in patients with long QT syndrome (LQTS) [9,12–14]. Long QT syndrome is a diseased syndrome in which the QT [see Fig. 1(a)] is longer than the normal values, which is caused by prolongation of the action potential duration (APD) in the heart. Recent computer simulation studies have shown that regional prolongation of APD can cause the second mechanism of arrhythmia initiation, i.e., spontaneous initiation of PVCs and reentry due to APD gradients [10,15–20]. However, a rigorous bifurcation analysis revealing the bifurcations leading to spontaneous arrhythmogenesis remains to be elucidated.

In this study we perform bifurcation analysis to investigate the instabilities promoted by repolarization gradients in a one-dimensional cable using a simple action potential model, the FitzHugh-Nagumo (FHN) model [21,22]. We carry out numerical simulations and linear stability analysis and show that a Hopf bifurcation leads to nonpropagating localized oscillations and then propagating excitations. Depending on the degree of heterogeneities, these excitations can range from one to many and can be sustained oscillations, manifesting as PVCs and sustained arrhythmias. The dynamics depends on the repolarization gradient and the length of the cable. Complex dynamics is also induced by the repolarization gradient. The mechanistic insights from the simple model may help in the understanding of the genesis of PVCs and arrhythmias in LQTS.

II. MODEL AND METHODS

The FHN model is a two-variable model, which is a generic model for excitable systems. Although it lacks the detailed

*schuangxd@scut.edu.cn

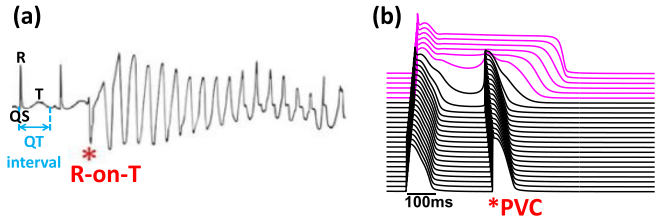

FIG. 1. The R-on-T phenomenon in the initiation of arrhythmias in LQTS. (a) Representative ECG showing R-on-T leading to ventricular arrhythmias. The sharp QRS wave corresponds to wavefront conduction in the heart. The domed T wave represents the repolarization phase of the heart. The time interval between the Q wave and the end of the T wave is called the QT interval, which is a measure of the repolarization of the heart. The red asterisk denotes an R wave superimposed on the T wave, called R-on-T, which is a typical ECG pattern preceding arrhythmias. This R wave is a PVC. (b) Time and space plot of voltage showing spontaneous PVC caused by regional prolongation of repolarization in a computer model of rabbit ventricular tissue [15].

physiological properties of cardiac myocytes, such as the ionic currents, it still captures some generic properties of excitation, repolarization, and recovery of cardiac myocytes. The one-dimensional cable model is described by the differential equations

$$\frac{\partial u}{\partial t} = \frac{u(1-u)(u-a)-v}{\epsilon} + D\nabla^2 u,$$
$$\frac{1}{\gamma}\frac{\partial v}{\partial t} = u - bv. \tag{1}$$

The variable u is an analog of the membrane voltage, v controls repolarization and recovery, D is the diffusion constant, a is a parameter determining the threshold of excitation, ϵ determines the excitability, γ controls the excitability and recovery, and b controls the decay of v, which then controls the speed of repolarization. When b is smaller than a critical value, u can repolarize normally, but when b is large enough, the system becomes bistable [see Fig. 2(a)]. Therefore, we model the repolarization heterogeneity by setting b as a function of space, i.e.,

$$b(x) = \begin{cases} b_L, & 0 < x \leqslant L_L \\ b_H, & L_L < x \leqslant L, \end{cases}$$

where the subscripts H and L stand for high and low, respectively, L_L and L_H are the lengths of the b_L and b_H regions, respectively, and $L = L_L + L_H$ is the total length of the cable. The setting is illustrated in Fig. 2(b). This heterogeneous cable can mimic cardiac tissue under the LQTS condition. First, a homogeneous stable resting state exists (despite physiological heterogeneity, all ventricular myocytes possess a nearly identical resting voltage). Second, the heterogeneity mimics the regional difference of repolarization in realistic ventricles. Note that in the H region of the 1D cable, the FHN model is bistable when uncoupled. This bistable behavior is equivalent to repolarization failure seen in cardiac myocytes under diseased conditions, such as heart failure and LQTS [23–27]. In other words, repolarization failure is a consequence of bistability. Moreover, it has been shown [28] that this same bistability is responsible for the very long action potential widely observed in experiments [23–27], which is facilitated by the slowly repolarizing currents in cardiac myocytes. However, there is no such slowly repolarizing component in the FHN model and thus we cannot simulate the very long action potential as seen in cardiac myocytes. On the other hand, in the heterogeneous 1D cable, due to diffusive coupling, the H region can still repolarize with very long action potential for a certain range of the b_H value (see Fig. 3). As shown in Appendix D, the dynamics of a 1D heterogeneous cable with the FHN model can well capture the dynamics of that with a more detailed cardiac action potential model. Hence the present model could be a proper model for excitation dynamics in ventricular tissue under the long QT condition.

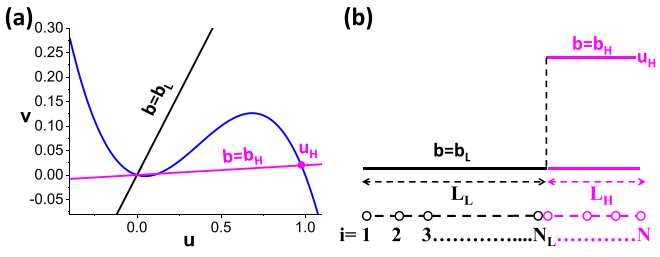

FIG. 2. The 1D cable model. (a) Nullclines of the FHN model. The slope of the straight line representing $u = bv$ determines excitable (black, labeled $b = b_L$) or bistable (magenta, labeled $b = b_H$) property. (b) Spatial heterogeneity of the cable. Unless specified, $b_H > 5.9211$ in the right magenta region (with a length of L_H) and $b_L < 5.9211$ in the left black region (with a length of L_L). For numerical simulation, the cable is discretized into N grid points as indicated at the bottom.

An explicit Euler method is used to integrate Eq. (1) with $\Delta t = 0.001$ and $\Delta x = 0.05$ and thus the number of the grid points is $N = L/\Delta x$ (a grid point can be regarded as a cell). The no-flux boundary condition is used. A single stimulus (with duration 0.01 and magnitude 30) is delivered to the b_H end [the Nth cell; see Fig. 2(b)] to initially excite the cable. Throughout the paper we fix $\epsilon = 0.01$, $D = 1.0$, and $a = 0.1$. Except in Secs. V and VI, $N_H = 50$ and $N_L = 100$ ($N = N_H + N_L = 150$) are fixed. Linear stability analysis of the steady state is carried out. The derivation of the steady-state solutions of an inhomogeneous cable is not a trivial task. We design a numerical method to search for all the solutions of the cable, which is demonstrated in Appendix A.

III. BIFURCATIONS TO TRANSIENT AND OSCILLATORY EXCITATIONS

This section investigates the bifurcations and different excitation behaviors of the 1D heterogeneous cable. Figure 3(a) shows the excitation behaviors in the b_H-b_L plane. Figures 3(b)–3(f) show typical excitation behaviors after a single stimulation for $b_L = 1.5$ and different b_H. When b_H is large [the green region (marked by roman numeral I) in Fig. 3(a)], repolarization fails in the b_H region but repolarizes normally in the b_L region [Fig. 3(b)]. Transient oscillations occur in the gradient region. When b_H is reduced [yellow region (II) in Fig. 3(a)], the oscillations in the gradient region

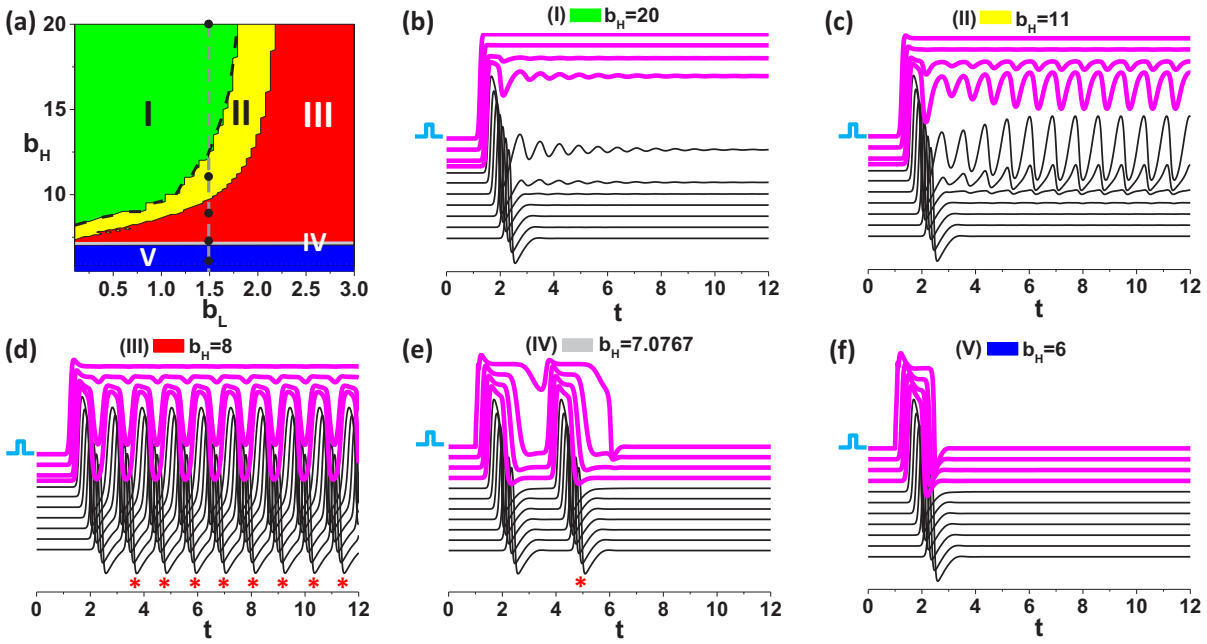

FIG. 3. Oscillatory behaviors induced by a repolarization gradient. (a) The b_H-b_L phase plane showing excitation behaviors, with $\gamma = 1$. The typical behaviors of different regions (also marked by roman numerals) are shown in (b)–(f). The black dashed curve separating the green (I) and yellow (II) regions is the Hopf bifurcation line obtained via bifurcation analysis. (b)–(f) Space-time plots of $u(x, t)$ for different b_H values marked on the vertical line in (a), with $b_L = 1.5$. The upper thicker magenta traces are $u(x, t)$ in the b_H region. The stimulus is delivered at $t = 1$ to the b_H-end cell. (b) Same as in (a) but with $b_H = 20$ in the stable steady state. (c) Same as in (a) but with $b_H = 11$ for regional oscillations without excitations. (d) Same as in (a) but with $b_H = 8$ for oscillations leading to propagating excitations. The spontaneous excitations are marked by the red asterisk. (e) Same as in (a) but with $b_H = 7.0767$ for transient excitations. (f) Same as in (a) but with $b_H = 6$ for normal repolarization in the whole cable.

become stationary; however, these oscillations cannot propagate out of the gradient region to form PVCs [Fig. 3(c)]. When b_H is reduced further [red region (III) in Fig. 3(a)], the oscillations propagate into PVCs [Fig. 3(d)]. In a very narrow region [gray (IV) in Fig. 3(a)], the b_H region can repolarize but still generates a single PVC [Fig. 3(e)]. When b_H is too small (region V), both the b_H and b_L regions repolarize normally [Fig. 3(f)]. The bifurcations leading to these states are detailed below.

When b_H is large enough (greater than 5.9211), there exist three steady states, as shown in Fig. 4(a), which can be solved numerically using the method mentioned in Sec. II (or Appendix A). They are labeled as F (green closed circles), S (red open circles below F), and Z (blue closed triangles at the bottom). Here Z is the trivial homogeneous zero solution (the resting state). As for F and S, linear stability analysis reveals that F is a focus, either stable or unstable depending on the parameters, and S is a saddle focus (see Appendix A for the calculated eigenvalues). Figure 4(b) shows the real parts of the largest eigenvalue of the F-associated Jacobian matrix λ_F (a complex number) and its complex conjugate vs b_H. As b_H is reduced, $\mathrm{Re}(\lambda_F)$ crosses zero to become positive [the critical point is labeled as HB in Fig. 4(b)], indicating that the F solution undergoes a Hopf bifurcation. This instability originates from the gradient region bordering the b_H and b_L regions [see Fig. 3(c) for the action potential and Figs. 4(c) and 4(d) for the bifurcation diagrams]. Although oscillations occur, these oscillations cannot propagate out of the middle region to form PVCs [see Fig. 4(d); $u(1)$ is quiescent despite oscillatory $u(90)$]. The oscillations propagate into PVCs when b_H is smaller than a critical value [labeled Exc in Figs. 4(c) and 4(d)] at which the amplitude of the limit cycle oscillation is large enough [see Fig. 3(d)]. As b_H is decreased further, transient excitations occur [see Fig. 3(e)], labeled TrE in Figs. 4(c) and 4(d). This transient zone [colored gray (region V) in Fig. 3(a)] is very narrow. When b_H becomes too small (equal to 5.9211), F and S annihilate via a saddle-node bifurcation, which is labeled SN in Figs. 4(c) and 4(d). The plots of steady-state F and S solutions just before annihilation are shown by the olive (solid) and pink (open) curves (denoted by F S collide), respectively, in Fig. 4(a). After this bifurcation, the spatially heterogeneous steady states F and S no longer exist in the cable. Therefore, for $b_H < 5.9211$ all the cells are allowed to repolarize and no gradient effect could be seen.

We carry out simulations in a heterogeneous 1D cable using a more physiologically detailed model, the Luo-Rudy (LR) model [29], and the results are presented in Fig. 11 in Appendix D. The excitation behaviors are almost the same as those obtained using the FHN model.

IV. COMPLEX EXCITATION DYNAMICS

Although γ does not vary the steady solutions, it affects the stability of the steady-state solutions and causes complex behaviors. Figure 5(a) shows the dynamics in the b_L-γ plane. The upper light gray region (VIII) is propagation failure, i.e., local excitations can never propagate out as an excitable wave in the cable. The rest of this plane can be divided into three

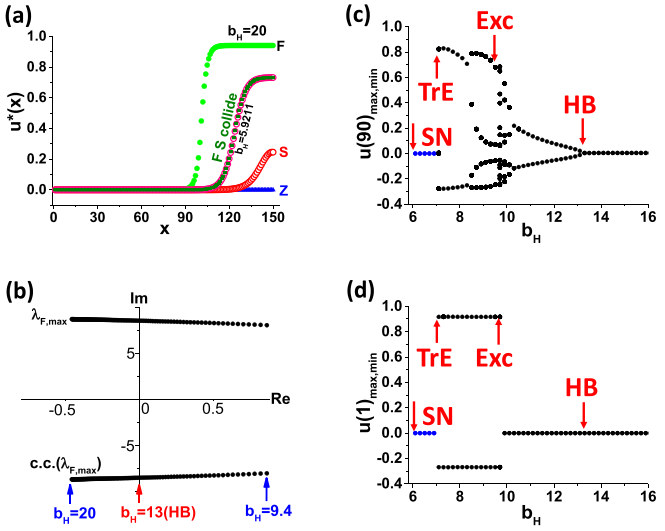

FIG. 4. Bifurcations leading to spontaneous excitations, with $b_L = 1.5$ and $\gamma = 1$. (a) Plot of the spatially heterogeneous steady-state solutions. The example of $b_H = 20$ is shown. There are three solutions, i.e., F (focus, green closed circles), S (saddle focus, red open circles), and Z (zero, blue closed triangles). If b_H is reduced to 5.9211, F and S will collide with each other, represented by the closed olive and open pink circles. (b) Largest (referring to the real part) eigenvalues of the F-associated Jacobian matrix vs b_H. Here HB denotes the Hopf bifurcation point. (c) Bifurcation diagram plotting u vs b_H for the 90th cell [denoted by $u(90)$]. The maximum and minimum u values of the stationary oscillations are recorded (the first 100 000 steps are discarded). Here Exc, TrE, and SN correspond to stationary excitation, transient excitation, and saddle-node bifurcation, respectively. (d) Same as in (c) but for the first cell [denoted by $u(1)$].

ranges based on the specific behaviors, i.e., small, intermediate, and large b_L, which are detailed below.

For very small b_L, i.e., $b_L < 1.1$, the F steady-state solution is permanently stable for any b_L and γ. For b_L between 1.1 and 1.65, varying γ can result in complex behaviors, such as quasiperiodicity, chaos, and multiattractors. A bifurcation diagram is shown in Fig. 5(b). As γ decreases, the system evolves continuously following the sequence of dynamics: stable focus → limit cycle → quasiperiodicity → chaos [see the black closed circles in Fig. 5(b) and the blowup in Fig. 5(c)]. These behaviors all bifurcate from the steady-state F solution. An interesting finding is that another attractor showing oscillatory excitations suddenly emerges at $\gamma = 0.4168$, which coexists with the F-associated oscillations. We use violet open circles in Figs. 5(a)–5(c) to denote this state. This type of excitation is associated with the S solution due to its saddle-focus property. Since F- and S-associated attractors coexist, a proper perturbation could switch the state between them, as shown in Fig. 5(d). With the reduction of γ the two attractors would approach each other and finally collide to give rise to robust excitations (see Appendix B for the estimation of the distance between them).

For intermediate b_L, the bifurcation to excitation is identical to that of varying b_H as introduced in Fig. 3, i.e., Hopf bifurcation gives rise to a limit cycle, and once its amplitude is large enough spontaneous PVCs could be elicited. For large b_L, multistability exists due to newly created steady-state solutions. Besides F, S, and Z, new steady-state solutions are created via a saddle-node bifurcation. All the spatially heterogeneous steady-state solutions are shown in the inset of Fig. 5(e), where the newly created solutions are named F' and S'. We choose the steady state of the first cell $[u^*(1)]$ vs b_L to show the change of the solution structure in Fig. 5(e), revealing a saddle-node bifurcation. For large b_L, the F solution is always unstable [denoted by the bottom smaller green open dots in Fig. 5(e)], whereas the stability of F' depends on the parameters. The largest (referring to the real part) eigenvalues of F', i.e., $\lambda(F')$ and c.c., vs γ are shown in Fig. 5(f), which reveals that F' loses its stability via a Hopf bifurcation. This Hopf bifurcation is subcritical, as shown in Fig. 5(g). Due to the subcritical property, there is a bistable region in which the stable steady-state F' solution and oscillations coexist. A space-time plot of $u(x,t)$ is shown in Fig. 5(h). If b_L is further increased to 5.9211, the excitable part also becomes bistable. At this point, solutions F and S' collide with each other and annihilate via a saddle-node bifurcation [labeled SN2 in Fig. 5(e)]. For $b_L > 5.9211$, only F', S, and Z exist. In this case, F' is just the steady state that connects the upper fixed point of both b_H and b_L parts of the tissue.

In the more physiologically detailed model (the LR model [29]), by altering the maximum conductance and the time constant of the time-dependent potassium current, we can reproduce the same complex behaviors (compare Figs. 3 and 5 with Fig. 11 in Appendix D). The similarity indicates that the bifurcation mechanisms leading to PVC using the FHN model can be extended to ventricular tissue.

V. EFFECTS OF CABLE LENGTH

The dynamical behaviors also depend on the cable length as well as the lengths of the two heterogeneous regions. Figure 6 shows the dependence of the dynamics on the cable length. Here $N_H = 50$ and $N_L = 100$ are the control lengths of the two regions. As shown in Fig. 6(a), as long as the cable is long enough, the dynamical behaviors are size independent. However, when either N_H or N_L is short, the dynamical behaviors become length dependent [e.g., the bifurcation point for $N_L = 15$ is different from those for longer cables; see Fig. 6(a)]. Figures 6(b) and 6(c) show the effects of N_H and N_L. Figure 6(b) reveals that N_H has little effect on the dynamics until N_H is too small, at which point F and S annihilate via a saddle-node bifurcation (indicated by the white dotted line). Figure 6(c) shows that the bifurcations depend on N_L to a greater degree. For $N_L \leqslant 12$, the F' solution no longer exists and only the F solution is present. Under this condition, as b_L is increased from small to large, the steady-state F solution would undergo a Hopf bifurcation twice, between which oscillatory excitations are present. For $8 < N_L \leqslant 12$ the Hopf bifurcation of F (indicated by the upper black dashed line bordering regions I and III) is subcritical, whereas for $N_L \leqslant 8$ it becomes supercritical. We show the two bifurcations in Appendix C. Figure 6(d) shows the dependence on the total length. Here $N_L = 2N_H$ is fixed, which presents a mixed effect of N_H and N_L. We can see that oscillations as well as PVCs could never occur in a short cable ($N \leqslant 18$). Therefore,

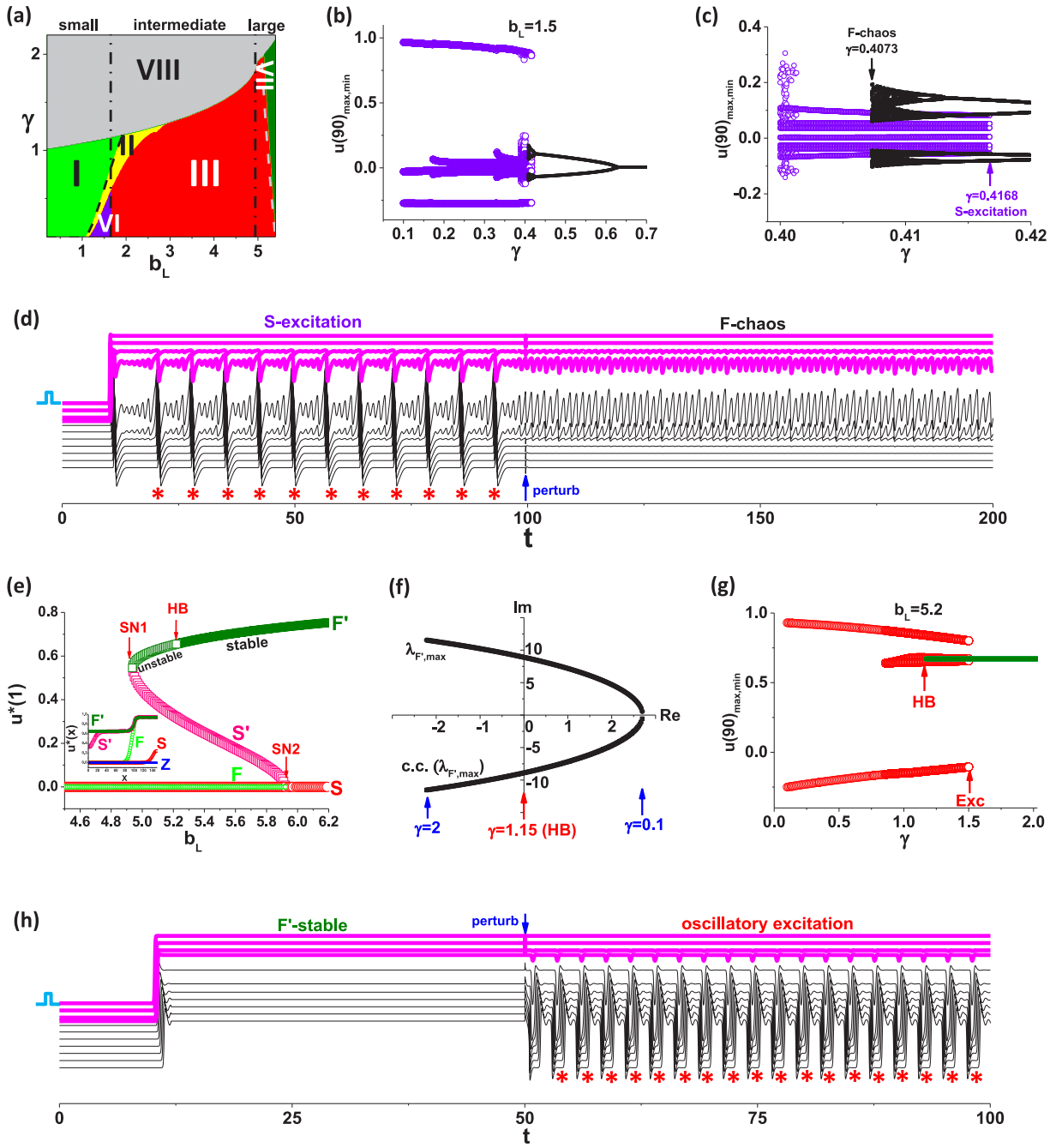

FIG. 5. Complex bifurcations and dynamics. Here $b_H = 20$ unless specified. (a) The b_L-γ phase plane. Based on the specific behaviors, the plane is divided into three regions, small, intermediate, and large b_L (separated by the vertical dash-dotted lines). Green (region I), yellow (II), and red (III) correspond to the same behaviors as in Fig. 3(a). Light gray (VIII), violet (VI), and olive (VII) represent propagation failure, S-associated oscillations, and stable steady-state F', respectively. The left black dashed curve is the Hopf bifurcation line of F, while the right light gray one is that of F' obtained via bifurcation analyses. (b) Bifurcation diagram showing $u(90)$ vs γ for small b_L ($b_L < 1.65$), with $b_L = 1.5$. The black closed circles are oscillations arising from the instability of the steady-state F solution, while the violet open circles are oscillations arising from the instability of the steady-state S solution. (c) Blowup of (b) for $\gamma \in (0.4, 0.42)$ showing the details of the F- and S-associated oscillations. At $\gamma = 0.4073$, the largest Lyapunov exponent of the F-chaos state is 6.13 (calculated by the method from [30]). (d) Space-time plot of $u(x, t)$ switching from the S-associated excitation state to the F-associated chaotic excitation state after a perturbation, with $\gamma = 0.4073$. The propagated excitations (or PVCs) are indicated by the red asterisk. (e) Solution structure vs b_L, with $\gamma = 1$. The steady-state u value of the first cell is shown. When $b_L = 4.94$, new steady-state solutions F' and S' are created via a saddle-node bifurcation, as indicated by SN1. An increase of b_L stabilizes F' via an inverse Hopf bifurcation, as indicated by HB. The inset shows the steady-state solutions for $b_L = 5.2$. At $b_L = 5.9211$, F and S' annihilate via a saddle-node bifurcation, labeled SN2. (f) Largest (referring to the real part) eigenvalues of the F'-associated Jacobian matrix vs γ. (g) Bifurcation diagram showing $u(90)$ vs γ for $b_L = 5.2$. The red open circles close to the olive solid F' branch are due to the small oscillations between successive PVCs, as shown in (h). (h) Space-time plot showing switching from the stable F' state to oscillatory excitation states after a perturbation, with $b_L = 5.2$ and $\gamma = 1.3$.

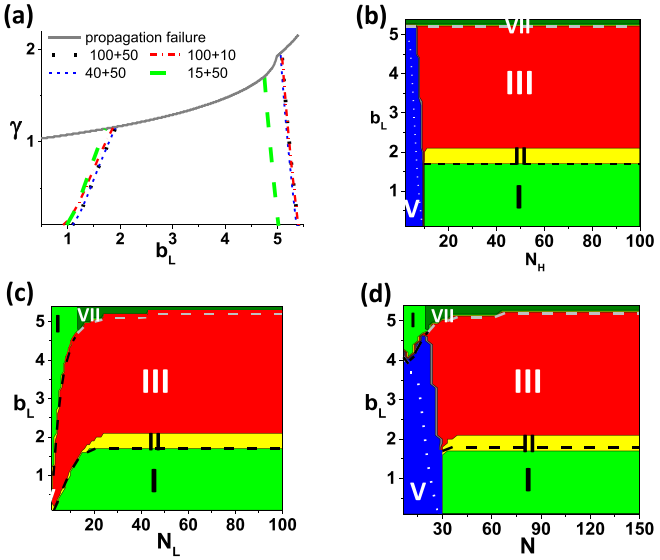

FIG. 6. Effects of the cable length, with $b_H = 20$ unless specified otherwise. (a) Dependence of the bifurcations on the cable length. Shown are the Hopf bifurcation points of F (left) and F' (right) on the b_L-γ plane for different cable lengths labeled as $N_L + N_H$. (b) Effect of N_H, with $N_L = 100$ fixed. The white dotted line indicates the annihilation of F and S. (c) Effect of N_L, with $N_H = 50$ fixed. Green (region I) is for stable F, while olive (region VII) is for stable F'. (d) Dependence on total length $N = N_H + N_L$, with $N_L = 2N_H$ fixed. If $N_L \leqslant 18$ the system stays stably on either F (green, I) or the homogeneous resting state (blue, V) and thus neither oscillations nor PVCs can occur.

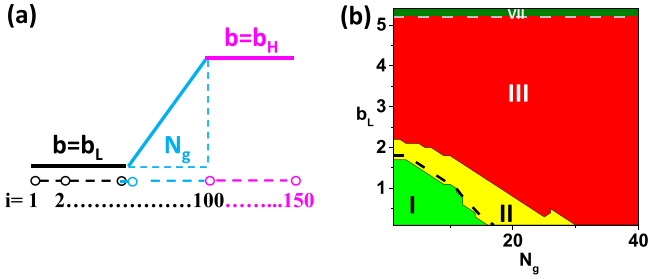

FIG. 7. Effects of the spatial gradient of parameter b, with $b_H = 20$ and $\gamma = 1$. (a) Configuration of the setting. The total length and the b_H region length are fixed at $N = 150$ and $N_H = 50$, respectively. The parameter b increases linearly from b_L to b_H within N_g cells. (b) Dynamical behaviors in the b_L-N_g plane. The lower black dashed curve indicates the Hopf bifurcation of the F solution obtained via stability analyses and the upper light gray dashed line is that of the F' solution.

the spontaneous PVCs or oscillations need a minimal length, indicating that these dynamics are a result of instabilities in a spatial system.

VI. ROLE OF the SPATIAL GRADIENT OF REPOLARIZATION

In a real biological system, the parameter change may not be so abrupt as we used above. Therefore, in this section we investigate the effect of the spatial gradient of the parameter. We set a gradient-adjustable region within the cable [Fig. 7(a)] in which b increases linearly from b_L to b_H within N_g points and thus the slope $(b_H - b_L)/N_g$ denotes the spatial gradient of b. We explore the behaviors in the b_L-N_g plane, as shown in Fig. 7(b). Increasing either b_L or N_g promotes the Hopf bifurcation of the steady-state F solution, but N_g has little effect on the stability of the steady-state F' solution. This indicates that reducing the gradient of b promotes oscillations, which agrees with the observation that reducing b_H promotes oscillations [Fig. 3(a)].

VII. SUMMARY

In the present paper we investigate the bifurcations leading to spontaneous excitations in an inhomogeneous FHN cable. The mechanistic insights from the bifurcation analysis may help in the understanding of the mechanisms for the genesis of PVCs and arrhythmias in LQTS. Our major findings are as follows.

(i) The mechanism of oscillatory excitation is via a Hopf bifurcation in a spatial system. The oscillations occur when b_H (the source) and b_L (the sink) are properly matched. The instability occurs in the gradient region via a supercritical Hopf bifurcation, first resulting in small-amplitude oscillations in the gradient region but no propagating PVCs. As the oscillation amplitude grows to a certain value, the oscillations propagate out of the gradient region to form PVCs.

(ii) More complex behaviors may occur depending on b_L and γ. Chaotic dynamics and multiple attractors occur for small b_L and γ, where excitations arise from instability of the steady-state S solution. On the other hand, large b_L gives rise to additional steady-state solutions (i.e., F' and S') via saddle-node bifurcation. The bifurcation of F' is a subcritical Hopf bifurcation.

(iii) The dynamics is also affected by the tissue size. The N_H (length of the source) maintains the repolarization gradient but has little effect on the dynamics, while N_L (length of the sink) influences the stability of the system. A minimum size is needed for the instability and spontaneous PVCs.

(iv) The spatial gradient of repolarization affects the stability of the F solution. Reducing the gradient promotes instability and spontaneous PVCs.

Note that in this simple FHN model, we can only have repolarization failure which mimics ultralong APD and repolarization failure in the cardiac system. As shown in our simulations, although the FHN model fails to repolarize when uncoupled, it can repolarize normally when coupled in tissue and can result in one or more PVCs or sustained oscillations. Furthermore as shown in many simulation and experimental studies [31–37], early afterdepolarizations (EADs) are a hallmark of LQTS, which cannot be modeled by the simple FHN model. Simulation studies have shown two mechanisms of PVC genesis [19,38]: An EAD-mediated one and an APD-gradient-mediated one. The EAD-mediated one occurs when the APD gradient is small, but the APD-gradient-mediated one is promoted by a large APD gradient. However, in the latter, whether EADs are present or not, the APD gradient is responsible primarily for the instabilities for PVC genesis. Therefore, although the FHN model cannot exhibit EADs,

instabilities caused by the repolarization gradient can still provide valuable mechanistic insights into the genesis of PVCs for LQTS, which need to be further investigated in more physiologically detailed models.

In conclusion, our results reveal that the spontaneous excitations that give rise to PVCs are a result of instabilities of a heterogeneous spatial system. The mechanistic insights from bifurcation analysis of the simple FHN model will provide a nonlinear dynamics foundation for the analysis of the genesis of PVCs in more realistic cardiac tissue models of LQTS.

ACKNOWLEDGMENTS

This work was supported by the Guangdong Basic and Applied Basic Research Foundation through Grant No. 2021A1515010500 (X.H.) and National Institutes of Health Grants No. R01 HL134709, No. R01 HL139829, and No. R01 HL157116 (Z.Q.).

APPENDIX A: DERIVATION AND PROPERTIES OF THE INHOMOGENEOUS STEADY STATES

We employ linear stability analysis to investigate the dynamical behaviors of the cable model. For stability analysis, we need to numerically obtain the steady-state solutions. The discretized version of Eq. (1) is

$$\begin{aligned}
\frac{du_1}{dt} &= f(u_1, v_1) + D\frac{u_2 - u_1}{\Delta x^2},\\
\frac{dv_1}{dt} &= g(u_1, v_1),\\
\frac{du_2}{dt} &= f(u_2, v_2) + D\frac{u_3 + u_1 - 2u_2}{\Delta x^2},\\
\frac{dv_2}{dt} &= g(u_2, v_2),\\
&\vdots\\
\frac{du_N}{dt} &= f(u_N, v_N) + D\frac{u_{N-1} - u_N}{\Delta x^2},\\
\frac{dv_N}{dt} &= g(u_N, v_N),
\end{aligned} \tag{A1}$$

where $f(u, v) = [u(1-u)(u-a) - v]/\epsilon$, $g(u, v) = \gamma[u - b(x)v]$, and the no-flux boundary condition is used. Setting $du_i/dt = dv_i/dt = 0$ $(i = 1, 2, \ldots, N)$, we obtain a set of algebra equations. We use the method shown in Fig. 8 to numerically solve all the steady-state solutions.

After obtaining the steady-state solutions, we substitute them into the associated Jacobian matrix and calculate the eigenvalues numerically. Here we show the eigenvalues of F, F', S, and S' for $b_H = 20$ and $\gamma = 1$ ($b_L = 1.5$ for F and S, and 5.4 for F' and S') to reveal their nature (only part of the

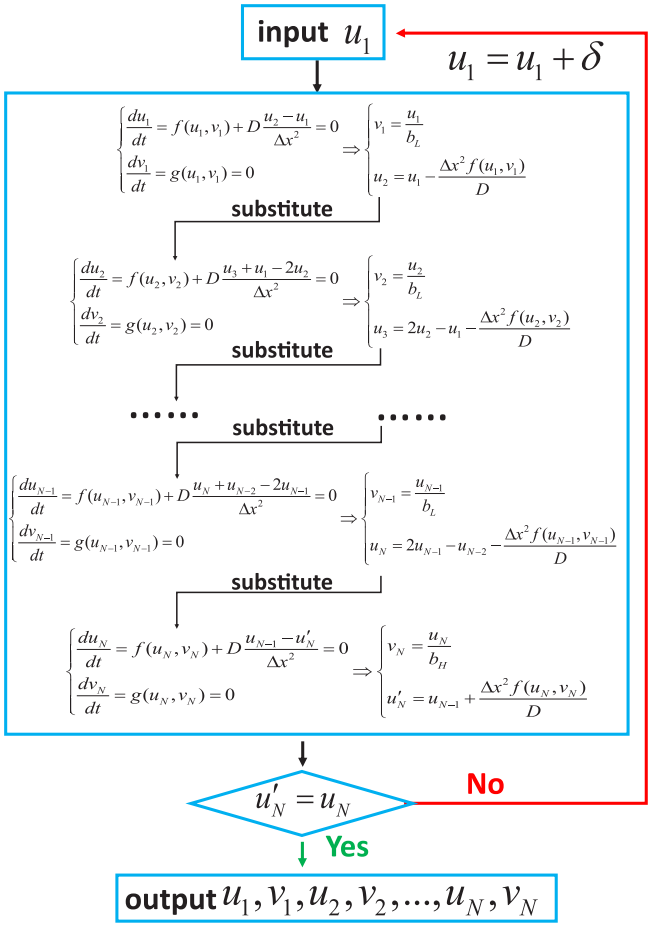

FIG. 8. Workflow for numerically solving the inhomogeneous steady-state solutions. Starting with a proper u_1 and solving the equations in sequence, one can finally get u_N. Substituting this u_N into the last equation would yield u'_N. If $u_N = u'_N$, the solution is self-consistent and the acquired $u_1, v_1, u_2, v_2, \ldots, u_N, v_N$ is the desired steady-state solution. If not, change another u_1 and repeat the process. By finely scanning u_1 (set the increment δ to be very small) we can numerically solve all the solutions.

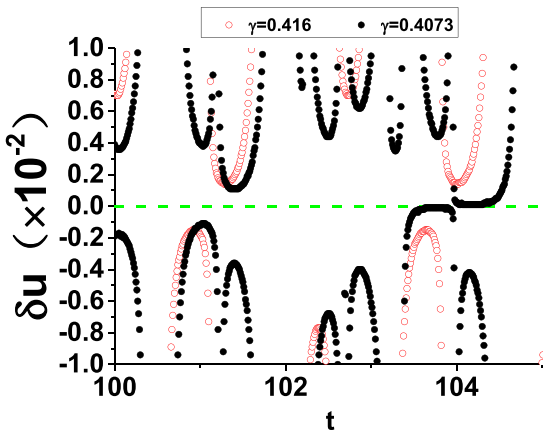

FIG. 9. Estimation of the distance between the F- and S-associated attractor for $b_L = 1.5$ and $b_H = 20$. The minimum $\delta u(t)$ enabling the switch from the F-associated attractor to the S-associated attractor is shown. The black closed circles are for $\gamma = 0.4073$ and the red open circles are for $\gamma = 0.416$.

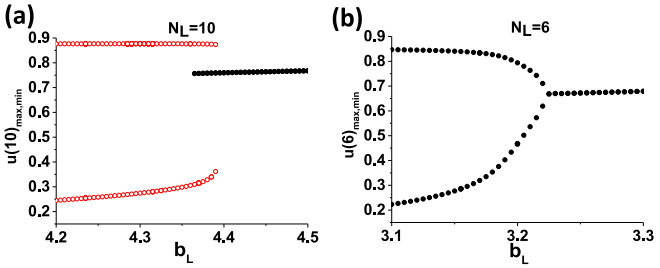

FIG. 10. Bifurcation types altered by N_L: (a) $N_L = 10$ for subcritical Hopf bifurcation and (b) $N_L = 6$ for supercritical Hopf bifurcation.

spectrum is shown and the largest ones are in bold font):

$$F: \begin{pmatrix} \cdots \\ -29.04791 \\ \mathbf{-0.45563 - 8.71363i} \\ \mathbf{-0.45563 + 8.71363i} \\ -5.80655 - 9.02384\mathbf{i} \\ -5.80655 + 9.02384\mathbf{i} \\ -6.25686 - 8.78508\mathbf{i} \\ -6.25686 + 8.78508\mathbf{i} \\ -7.98882 \\ \cdots \end{pmatrix}, S: \begin{pmatrix} \cdots \\ \mathbf{15.84393} \\ -38.79375 \\ -33.07309 \\ -23.98613 - 6.72988\mathbf{i} \\ -23.98613 + 6.72988\mathbf{i} \\ -25.80644 - 1.59644\mathbf{i} \\ -25.80644 + 1.59644\mathbf{i} \\ -22.11294 \\ \cdots \end{pmatrix},$$

$$F': \begin{pmatrix} \cdots \\ -31.19967 \\ \mathbf{-2.46743 - 9.56032i} \\ \mathbf{-2.46743 + 9.56032i} \\ -2.92411 - 9.68853\mathbf{i} \\ -2.92411 + 9.68853\mathbf{i} \\ -3.80936 - 9.87226\mathbf{i} \\ -3.80936 + 9.87226\mathbf{i} \\ -22.13624 \\ \cdots \end{pmatrix}, S': \begin{pmatrix} \cdots \\ \mathbf{21.83322} \\ -43.36554 \\ -34.66603 \\ -2.69446 - 9.62698\mathbf{i} \\ -2.69446 + 9.62698\mathbf{i} \\ -3.57067 - 9.83087\mathbf{i} \\ -3.57067 + 9.83087\mathbf{i} \\ -22.29721 \\ \cdots \end{pmatrix}.$$

As the parameters are changed, F and F' undergo Hopf bifurcation [as shown in Figs. 4(b) and 5(f)], while S and S' retain their saddle-focus properties.

APPENDIX B: ESTIMATION OF DISTANCE BETWEEN F- AND S-ASSOCIATED ATTRACTORS

In Sec. IV we showed that there are coexisting F- and S-associated attractors for small b_L. With the reduction of γ they approach each other and finally merge to form robust PVCs. The approaching of the attractors could be indicated by the distance between them, which is estimated in the following way. In the multiattractor parameter range, if we perturb all u simultaneously at a certain time, i.e., $u(x,t) = u(x,t) + \delta u(t)$, the system would switch between the attractors. The minimum $\delta u(t)$ enabling the switch could roughly estimate the distance between the attractors. Figure 9 shows that the minimum $\delta u(t)$ on $\gamma = 0.4073$ is very close to 0 at certain time moments, much less than that of a little bit larger γ. This

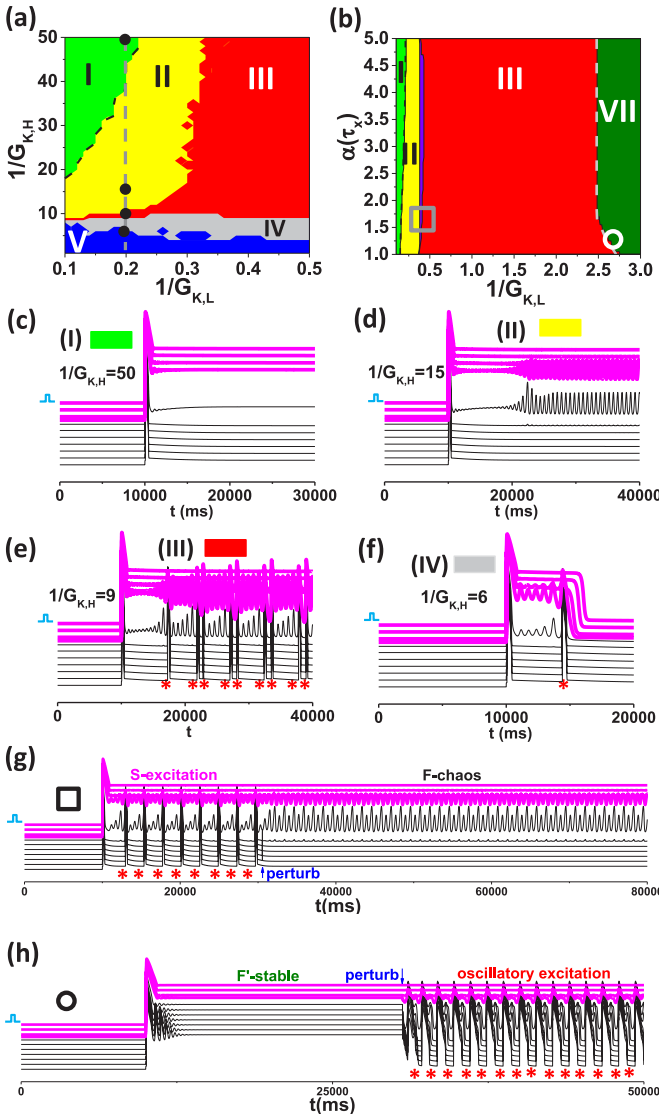

FIG. 11. Excitation dynamics in a heterogeneous 1D cable using the LR model, with $G_{si} = 0.2$ mS/cm^2. The stimulus (pulse duration of 2 ms and magnitude of 50 μA/cm^2) is delivered to the upper $G_{K,H}$-end cell at $t = 10$ s. (a) Dynamical behaviors on the $1/G_{K,L}$-$1/G_{K,H}$ plane, with $\alpha(\tau_X) = 10$. The colors and numbers are the same as in Fig. 3(a). The space-time plots of voltage for the parameter values marked on the gray dashed vertical line are shown in (c)–(f). (b) Dynamical behaviors on the $1/G_{K,L}$-$\alpha(\tau_X)$ plane, with $G_{K,H} = 0.01$ mS/cm^2. The colors and numbers are the same as in Fig. 5(a). The space-time plots for the parameters marked by the square and circle are shown in (g) and (h), respectively. (c) Plot of $(1/G_{K,L}, 1/G_{K,H}) = (0.2, 50)$. (d) Plot of $(1/G_{K,L}, 1/G_{K,H}) = (0.2, 15)$. (e) Plot of $(1/G_{K,L}, 1/G_{K,H}) = (0.2, 9)$. (f) Plot of $(1/G_{K,L}, 1/G_{K,H}) = (0.2, 6)$. (g) Space-time plot of the voltage of multiple solutions, similar to Fig. 5(d), with $G_{K,H} = 0.01$ mS/cm^2, $G_{K,L} = 2.5$ mS/cm^2, and $\alpha(\tau_X) = 1.7$. (h) Bistable states of F and oscillatory excitations, similar to Fig. 5(h), with $G_{K,H} = 0.01$ mS/cm^2, $G_{K,L} = 0.37$ mS/cm^2, and $\alpha(\tau_X) = 1.1$.

means that as γ is reduced, the distance between the attractors is reduced.

APPENDIX C: BIFURCATION TYPES ALTERED BY N_L

In Sec. V we found that the length of the b_L region (N_L) can alter the bifurcation type when it is small. Here we show more details about this by showing the bifurcation diagram plotting u vs b_L, as shown in Fig. 10. For $N_L = 10$ [Fig. 10(a)], there exists a range where stable F and oscillatory excitation can both be stably present, which is a typical characteristic of subcritical Hopf bifurcation. For $N_L = 6$ [Fig. 10(b)], the situation is different: A supercritical Hopf bifurcation occurs.

APPENDIX D: SIMILAR RESULTS USING THE LR MODEL

In order to extend the FHN results to a more realistic cardiac model, we employ a more detailed physiology model, i.e., the LR model [29], to study the PVC behaviors. This model describes the action potential of guinea pig ventricular myocytes and has been widely used to investigate fundamental mechanisms of arrhythmias. The setting of the 1D cable is similar to the one with the FHN model and the heterogeneity is modeled by changing G_K (the maximum potassium current conductance) as follows [15,38]:

$$G_K(x) = \begin{cases} G_{K,L}, & 0 < x \leqslant L_L \quad \text{(excitable)} \\ G_{K,H}, & L_L < x \leqslant L \quad \text{(bistable)}. \end{cases}$$

We also alter the maximum conductance (G_{si}) of the slow inward current and the time constant of the X gate [using $\alpha(\tau_X)$ as the multiplied factor]. The other parameters are set at their default values in the original model (see [29]).

We investigated the behaviors in the $1/G_{K,L}$-$1/G_{K,H}$ and $1/G_{K,L}$-$\alpha(\tau_X)$ planes [see Figs. 11(a) and 11(b)]. The pictures are similar to Figs. 3(a) and 5(a). This further indicates that the parameter b corresponds to the conductance of potassium current and γ plays a similar role of repolarizing kinetics. However, note that the multiattractor ranges are much narrower in the LR model. Figures 11(c)–11(f) are space-time plots of voltage from different regions in Fig. 11(a), showing almost the same behaviors as in Fig. 3. Figures 11(g) and 11(h) show complex excitation behaviors of the LR model, where the multiple solutions and F'-associated PVCs are present, similar to the ones shown in Fig. 5. These complex behaviors occur at large $1/G_{K,H}$, meaning that the potassium current is small.

[1] D. P. Zipes and H. J. Wellens, Circulation **98**, 2334 (1998).
[2] Z. Qu and J. N. Weiss, Annu. Rev. Physiol. **77**, 29 (2015).
[3] A. T. Winfree, Sci. Am. **248**(5), 144 (1983).
[4] A. Karma, Annu. Rev. Condens. Matter Phys. **4**, 313 (2013).
[5] Z. Qu, G. Hu, A. Garfinkel, and J. Weiss, Phys. Rep. **543**, 61 (2014).
[6] T.-C. Chou and F. Wenzke, Am. Heart J. **96**, 191 (1978).
[7] J. A. Chiladakis, G. Karapanos, P. Davlouros, G. Aggelopoulos, D. Alexopoulos, and A. S. Manolis, Am. J. Cardiol. **85**, 289 (2000).
[8] T. R. Engel, S. G. Meister, and W. S. Frankl, Ann. Internal Med. **88**, 221 (1978).
[9] C. Lerma, C. F. Lee, L. Glass, and A. L. Goldberger, J. Electrocardiol. **40**, 78 (2007).
[10] M. B. Liu, N. Vandersickel, A. V. Panfilov, and Z. Qu, Circ. Arrhythm. Electrophysiol. **12**, e007571 (2019).
[11] Z. Qu, M. B. Liu, R. Olcese, H. Karagueuzian, A. Garfinkel, P.-S. Chen, and J. N. Weiss, Heart Rhythm **19**, 1369 (2022).
[12] B. J. Drew, M. J. Ackerman, M. Funk, W. B. Gibler, P. Kligfield, V. Menon, G. J. Philippides, D. M. Roden, and W. Zareba, Circulation **121**, 1047 (2010).
[13] H. Morita, J. Wu, and D. P. Zipes, Lancet **372**, 750 (2008).
[14] M. Badri, A. Patel, C. Patel, G. Liu, M. Goldstein, V. M. Robinson, X. Xue, L. Yang, P. R. Kowey, and G.-X. Yan, JACC Clin. Electrophysiol. **1**, 315 (2015).
[15] X. Huang, T. Y. Kim, G. Koren, B.-R. Choi, and Z. Qu, Am. J. Physiol. Heart Circ. Physiol. **311**, H1470 (2016).
[16] W. Liu, T. Y. Kim, X. Huang, M. B. Liu, G. Koren, B.-R. Choi, and Z. Qu, J. Physiol. **596**, 1341 (2018).
[17] A. S. Teplenin, H. Dierckx, A. A. F. de Vries, D. A. Pijnappels, and A. V. Panfilov, Phys. Rev. X **8**, 021077 (2018).
[18] N. Vandersickel, T. P. de Boer, M. A. Vos, and A. V. Panfilov, J. Physiol. **594**, 6865 (2016).
[19] Z. Zhang, M. B. Liu, X. Huang, Z. Song, and Z. Qu, Biophys. J. **120**, 352 (2021).
[20] S. Heitmann, A. Shpak, J. I. Vandenberg, and A. P. Hill, PLoS Comput. Biol. **17**, e1008683 (2021).
[21] R. FitzHugh, Biophys. J. **1**, 445 (1961).
[22] J. Nagumo, S. Arimoto, and S. Yoshizawa, Proc. IRE **50**, 2061 (1962).
[23] F. L. Puisieux, M. M. Adamantidis, B. M. Dumotier, and B. A. Dupuis, British J. Pharmacol. **117**, 1377 (1996).
[24] I. A. Undrovinas, A. V. Maltsev, and N. H. Sabbah, Cell. Mol. Life Sci. **55**, 494 (1999).
[25] C. Antzelevitch, Eur. Heart J. **3**, K2 (2001).
[26] P. M. R. Orth, J. C. Hesketh, C. K. H. Mak, Y. Yang, S. Lin, G. N. Beatch, A. M. Ezrin, and D. Fedida, Cardiovasc. Res. **70**, 486 (2006).
[27] S. Kettlewell, P. Saxena, J. Dempster, M. A. Colman, R. C. Myles, G. L. Smith, and A. J. Workman, J. Physiol. **597**, 3619 (2019).
[28] Z. Qu and D. Chung, PLoS One **7**, e43587 (2012).
[29] C. H. Luo and Y. Rudy, Circ. Res. **68**, 1501 (1991).
[30] G. Benettin, L. Galgani, A. Giorgilli, and J.-M. Strelcyn, Meccanica **15**, 21 (1980).
[31] Z. Qu, L.-H. Xie, R. Olcese, H. S. Karagueuzian, P.-S. Chen, A. Garfinkel, and J. N. Weiss, Cardiovasc. Res. **99**, 6 (2013).
[32] C. T. January, J. M. Riddle, and J. J. Salata, Circ. Res. **62**, 563 (1988).

[33] N. El-Sherif, W. Craelius, M. Boutjdir, and W. B. Gough, J. Cardiovasc. Electrophysiol. **1**, 145 (1990).
[34] G.-X. Yan, Y. Wu, T. Liu, J. Wang, R. A. Marinchak, and P. R. Kowey, Circulation **103**, 2851 (2001).
[35] D. X. Tran, D. Sato, A. Yochelis, J. N. Weiss, A. Garfinkel, and Z. Qu, Phys. Rev. Lett. **102**, 258103 (2009).
[36] N. Vandersickel, I. V. Kazbanov, A. Nuitermans, L. D. Weise, R. Pandit, and A. V. Panfilov, PLoS One **9**, e84595 (2014).
[37] X. Huang, Z. Song, and Z. Qu, PLoS Comput. Biol. **14**, e1006382 (2018).
[38] Z. Zhang and Z. Qu, Phys. Rev. E **103**, 062406 (2021).